TOMOGRAPHIC RECONSTRUCTION OF DIFFUSION PROPAGATORS FROM DW-MRI USING OPTIMAL SAMPLING LATTICES

Wenxing Ye, Alireza Entezari, Baba C. Vemuri

CISE Department, University of Florida, Gainesville, FL 32611-6120, USA

ABSTRACT

This paper exploits the power of optimal sampling lattices in tomography based reconstruction of the diffusion propagator in diffusion weighted magnetic resonance imaging (DW-MRI). Optimal sampling leads to increased accuracy of the tomographic reconstruction approach introduced by Pickalov and Basser [1]. Alternatively, the optimal sampling geometry allows for further reducing the number of samples while maintaining the accuracy of reconstruction of the diffusion propagator. The optimality of the proposed sampling geometry comes from the information theoretic advantages of sphere packing lattices in sampling multidimensional signals. These advantages are in addition to those accrued from the use of the tomographic principle used here for reconstruction. We present comparative results of reconstructions of the diffusion propagator using the Cartesian and the optimal sampling geometry for synthetic and real data sets.

Index Terms— Optimal Sampling Lattices, Diffusion Propagator, DW-MRI, Tomography

1. INTRODUCTION

Diffusion MRI is a non-invasive imaging technique that exhibits sensitivity to Brownian motion of water molecules through tissue *in vivo*. Water molecules exhibit preferred directional diffusion through tissue rich in white matter fibers. This directional preference allows one to infer connectivity patterns as well as changes in them over time that can be used in various clinical applications. Diffusion tensor MRI (DT-MRI or DTI), introduced by [2], gives a relatively simple way of characterizing diffusional anisotropy and predicting the local fiber orientation within the tissue from diffusion weighted MRI data. DTI assumes that the diffusion propagator function is characterized by an oriented Gaussian probability distribution function. It is now well known that this model fails to capture complex geometries caused by crossing, kissing or splaying fibers that result in orientational heterogeneity [3] in a voxel. This has spurred the development of improved acquisition techniques and reconstruction methods. By sampling the diffusion signal on a 3D Cartesian lattice, the $\mathbf{q}$-space imaging (QSI) technique, also referred to as diffusion spectrum imaging (DSI) [4], uses the Fourier relation between the diffusion signal and the diffusion propagator (probability density function (PDF)) $P(\mathbf{r})$ [5]: $S(\mathbf{q}) = S_0 \int_{\mathbb{R}^3} P(\mathbf{r})\, e^{i\mathbf{q}\cdot\mathbf{r}} \mathrm{d}\mathbf{r}$, where $\mathbf{r}$ is the displacement vector, $\mathbf{q} = \gamma\delta\mathbf{G}$, γ is the gyromagnetic ratio, δ is the duration of diffusion gradient and $\mathbf{G}$ is the diffusion gradient. The sampling burden in QSI however makes the acquisition time-intensive and limits its widespread application. In [3], Tuch *et al* developed a clinically feasible approach called high angular resolution diffusion imaging (HARDI), in which apparent diffusion coefficients, D_{app}, are measured along many directions. In the presence of intra-voxel heterogeneity, several studies proposed to represent the diffusivity function using higher order Cartesian tensors leading to a generalization of DTI [6, 7]. Another class of techniques attempt to capture a compromised version of $P(\mathbf{r})$, the so called q-ball imaging (QBI) method, in which the radial integral of the displacement PDF is approximated by the spherical Funk-Radon transform [3, 8]. Finally, another class of methods that approximate the intra-voxel heterogeneity using a deconvolution approach assuming a continuous distribution to capture the mixing density associated with the fiber population within a voxel, details of can be found in [9, 10].

In this paper, we propose a model-free approach to reconstruction of the diffusion propagator at each voxel. The approach builds on the work in Pickalov and Basser [1], where in they exploit the Fourier transform relationship between $P(\mathbf{r})$ and $S(\mathbf{q})$ to develop a tomographic reconstruction of the propagator at each voxel. By interpolating a relatively small number of samples from the DW signal in the $\mathbf{q}$-space onto a regular grid, their approach allows for a tomographic reconstruction of $P(\mathbf{r})$ using the Fourier transform.

Since $P(\mathbf{r})$, at each voxel (tile), may contain anisotropic features in *any* arbitrary direction, it behooves us to choose a tiling of the space where each tile captures the maximum radial content of $P(\mathbf{r})$. Optimal tiling of the space results in voxels that admit a larger inscribing sphere compared to the traditional Cartesian tiling with cubic voxels. The main idea in this paper exploits optimal tiling where each voxel is a rhombic dodecahedron and admits a larger inscribing sphere; hence, a better resolution of $P(\mathbf{r})$ (i.e., the one with a larger radius $\mathbf{r}$) is available with the same sampling density as with

This research was supported by the NIH grant EB007082 to Baba Vemuri.

cubic Cartesian tiling. The rhombic dodecahedral tiling centers form the Face Centered Cubic (FCC) lattice which is the densest sphere packing lattice in 3-D. As we will see in the Section 2, this amounts to optimal sampling of the $\mathbf{q}$-space on a Body Centered Cubic (BCC) lattice which is the key contribution of our work. The optimal sampling in $\mathbf{q}$-space allows us to achieve a better reconstruction due to significantly smaller ghosting effects in the reconstructed $P(\mathbf{r})$.

Additionally, by using a significantly reduced sample set, we can maintain the same accuracy as one obtained using a Cartesian sampling lattice. We present evidence of these advantages via experiments on synthetic data as well as a real DW-MRI data.

2. OPTIMAL SAMPLING LATTICES

When sampling a multi-D signal on a given lattice, the spectrum of the sampled signal is replicated on the reciprocal lattice, where the original lattice and reciprocal lattice are Fourier transform pairs (in the distributional sense). The spectrum of the signal is contained in the **Brillouin zone** which is the Voronoi cell of the reciprocal lattice. The multi-D version of the Nyquist frequency is the boundary of the Brillouin zone. The Cartesian lattice is the reciprocal of itself. While in 2-D hexagonal lattice is also reciprocal to itself, in 3-D the BCC and FCC lattices are reciprocal to each other.

When it comes to sampling multi-dimensional signals, the Cartesian lattice is almost always the discretization of choice due to its simplicity; moreover, most of the 1-D signal processing algorithms can easily be extended to 2-D or 3-D or higher dimensions by a tensor-product approach. However, the Cartesian lattice has been known to be an inefficient lattice from the sampling-theory point of view. Petersen and Middleton [11] were among the first people to discover the superiority of sphere-packing and sphere-covering lattices for sampling multi-dimensional signals. In particular they have demonstrated that the Cartesian lattice is very inefficient for sampling multi-dimensional signals, especially in three-dimensions and higher. From an information theoretic point of view these lattices are the the ideal lattices for sampling stationary isotropic random processes [12].

In the 2-D setting the hexagonal lattice is the best sampling lattice since its reciprocal lattice, which happens to be the dual hexagonal lattice, allows for the best packing of 2-D with discs. When compared to the commonly-used Cartesian lattice with the same sampling density, the hexagonal lattice allows for about 14% more information to be captured in the spectrum of the underlying signal. For the case of $\mathbf{q}$-space sampling the spectrum of the sampled signal is $P(\mathbf{r})$ which is contained inside the pixel in the space domain which is the Voronoi cell (tiling) of the dual lattice. This is illustrated in Figure 1 as the area of inscribing disc to the Brillouin zone of the hexagonal lattice (i.e., hexagon) is larger than the area of inscribing disc to the Brillouin zone of the Cartesian lattice (i.e., square), while the two Brillouin zones have the unit area.

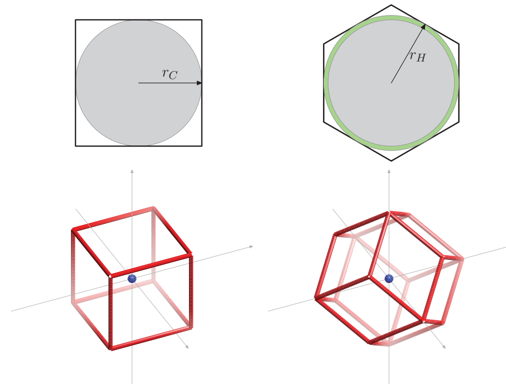

Fig. 1. First row: A square and a hexagon pixels with unit area corresponding to the Brillouin zone of Cartesian and hexagonal sampling in $\mathbf{q}$-space. The area of inscribing disc to a square is about 14% less than the area of the inscribing disc to the hexagon. Second row: In 3-D, this difference is about 30%, comparing a cubic voxel to rhombic-dodecahedron, the voxel of the FCC lattice, with the same volume.

In a 3-D setting, the optimal sampling lattice is the BCC lattice whose reciprocal lattice (i.e., the FCC lattice) is the densest sphere packing lattice. The sampling efficiency of the BCC lattice, when compared to the commonly-used Cartesian lattice is about 30% higher. Therefore, when sampling $\mathbf{q}$-space $E(\mathbf{q})$ on a BCC lattice, the $P(\mathbf{r})$ is contained in rhombic dodecahedral voxels which admit a larger inscribing sphere than the commonly used Cartesian voxels. The inscribing sphere to the rhombic dodecahedral voxel is about 30% larger than that of the cubic voxel while the two voxels are of the same unit volume. Therefore, when reconstructing $P(\mathbf{r})$ on each individual voxel, a reconstruction based on BCC sampling of $\mathbf{q}$-space yield larger resolution of $\mathbf{r}$ while preventing the ghosting artifacts. The ghosting artifacts is the space-domain equivalent of aliasing. When sampling the $\mathbf{q}$-space signal in frequency space with a coarse sampling rate, the replicas in the space domain bleed into the main voxel area. For a given fixed sampling resolution in $\mathbf{q}$-space, the ghosting artifact is smaller for the rhombic dodecahedral voxel compared to the commonly-used cubic voxels. This is due to the optimal sphere packing of the FCC lattice (with a rhombic dodecahedral voxel) compared to the Cartesian lattice (with a cubic voxel).

3. ALGORITHM AND IMPLEMENTATION

The algorithm proposed by Pickalov and Basser [1] is a modified version of the iterative procedure presented by Gerchberg and Papoulis (G-P). They assume the original data samples lie on radial lines in $\mathbf{q}$-space. On each radial line, several samples are available corresponding to different radii. Using an interpolator/extrapolator, they obtain the data values on a Cartesian lattice in the $\mathbf{q}$-space. By imposing some constrains both in the $\mathbf{q}$-space and displacement probability -space, their algorithm runs iteratively via the use of direct and inverse Fourier transforms. In each iteration, the original sampled data is imposed into the $\mathbf{q}$-space values to reinforce the consistency between the reconstructed $P(\mathbf{r})$ and the true diffusion propagators implied by the data samples.

As we saw in Section 2 we can increase the accuracy of reconstruction by changing the $\mathbf{q}$-space sampling from the Cartesian lattice to the BCC lattice. Therefore, we push the radially sampled data, on to the BCC lattice together with an approach similar to the algorithm of Pickalov and Basser. Since our purpose is to investigate the theoretical advantages of the optimal lattice, we took the same radial samples from $E(\mathbf{q})$ and pushed them into both Cartesian and BCC lattices with the same number of lattice points. While there are several esoteric interpolation methods [13] for interpolation into the BCC and Cartesian lattices, we used an identical interpolant in both cases to ensure that the only difference in the two reconstructions is the sampling geometry. Therefore, we used a cubic spline interpolant in both cases, even though in our experiments, other interpolants resulted in similar results.

After the Cartesian and BCC re-sampling of the $\mathbf{q}$-space data, the $P(\mathbf{r})$ reconstruction is obtained through a direct Fourier transform. While the usual FFT algorithm is suitable for Cartesian sampling, the we employed the modified FFT algorithm [14] for the BCC sampled data. In order to evaluate our method the accuracy of reconstruction in each case was measured by comparing the reconstructed signal from the true synthetic signal by the means of sum of squared errors (SSE). For the synthetic data some visual comparison is insightful and discussed in Section 4.

4. EXPERIMENTS

We now present propagator reconstruction experiments using the BCC and Cartesian lattices in a synthetic dataset (Figure 2) and a real dataset (Figure 3) from a rat optic chiasm.

N_r	10	9	8	7	6
Cartesian($\times 10^{-5}$)	2.19	2.31	2.63	3.34	4.04
BCC($\times 10^{-5}$)	0.60	0.68	0.87	1.38	2.56

Table 1. SSE comparison of reconstructions from different lattices with N_r, $N_\theta = 12$, $N_\phi = 13$, $\alpha = 90°$

For our synthetic data experiments, we generated samples from a mixture of two Gaussian functions in the 3-D $\mathbf{q}$-space and examined the SSE between reconstructions and the true signal. In the experiments, data samples are distributed on radial lines along (r, θ, ϕ) in the spherical coordinate system. The number of samples along each radial line is denoted by N_r, of θ values by N_θ, and the ϕ values by N_ϕ respectively. α denotes the angle between the two Gaussian components.

N_θ, N_ϕ	12,13	11,12	10,11	9,10	8,9
Cartesian($\times 10^{-5}$)	2.19	3.91	6.67	5.40	3.36
BCC($\times 10^{-5}$)	0.60	1.37	3.83	2.81	2.97

Table 2. SSE comparison of reconstructions from different lattices with $N_\theta, N_\phi, N_r = 10, \alpha = 90°$

α	90°	80°	70°	60°	50°
Cartesian($\times 10^{-5}$)	2.19	3.75	4.16	4.04	2.92
BCC($\times 10^{-5}$)	0.60	1.05	1.60	2.09	1.69

Table 3. SSE comparison of reconstructions from different lattices with α, $N_r = 10$, $N_\theta = 12$, $N_\phi = 13$

Table 1 reports the SSE differences between the BCC and Cartesian reconstructions with fixed $\alpha = 90°$ and varying N_r. It is evident from the errors that the BCC-based reconstruction yields smaller errors despite the same sampling rate N_r as in the Cartesian-based reconstruction; this remains to be the case even for varying sampling resolutions. Similarly by changing the sampling resolutions in N_θ and N_ϕ, the advantages of BCC reconstruction is maintained (see Table 2). Table 3 depicts the comparison between BCC and Cartesian reconstructions by varying the angle between the two Gaussian components simulating various angles of fiber-crossings. Table 4 compares the reconstructions under additive Rician noise of different noise levels σ. We can clearly see that under all the test conditions, reconstructions from BCC lattice achieve smaller errors compared to reconstructions from the Cartesian lattice. Also, Table 1 and Table 2 show that a reconstruction based on a smaller number of BCC samples (e.g., $N_r = 6$) in the $\mathbf{q}$-space is comparable to a reconstruction with larger number of Cartesian samples (e.g., $N_r = 8$) in the q-space. This suggests a strategy to further reduce the sample size of $E(\mathbf{q})$ and reduce the acquisition time.

For $N_r = 10$, $N_\theta = 12$, $N_\phi = 13$, $\alpha = 80$ and $\sigma = 0$, Figure 2 shows the isosurfaces of the reconstructed $P(\mathbf{r})$ from Cartesian and BCC lattices respectively. We can see that the isosurface of $P(\mathbf{r})$ from Cartesian lattice exhibits some ghosting artifacts at the tips due to leakage from ghosts in the neighboring period. The reconstruction from BCC lattice is not influenced by the ghosting artifacts since when we take samples on BCC lattice in $\mathbf{q}$-space, the distance between the reconstructed $P(\mathbf{r})$ and its nearest ghost replica is larger than

σ	0	0.02	0.04	0.06	0.08
Cartesian($\times 10^{-5}$)	2.19	2.57	3.51	4.79	6.78
BCC($\times 10^{-5}$)	0.60	1.05	2.31	3.84	6.28

Table 4. SSE comparison of reconstructions from different lattices with σ, $N_r = 10$, $N_\theta = 12$, $N_\phi = 13$, $\alpha = 90$

that derived from Cartesian lattice. Theoretically, the larger distance implies less influence from the ghost replica.

We now present an experiment with real data from a rat optic chiasm, which contains samples measured with 46 different directions with just one b value. Since our algorithm needs samples with different b values, for interpolation purposes, we used the high rank tensor model in [7] to process the data and get the values for different bs via re-sampling. Figure 3 depicts the probability maps reconstructed from the Cartesian and BCC lattices respectively. A close examination depicts that the reconstruction from Cartesian lattice appears distorted compared to the BCC reconstruction. This is due to the resilience of the BCC sampling (of $\mathbf{q}$-space) to the ghosting artifacts that distort the reconstruction of $P(\mathbf{r})$.

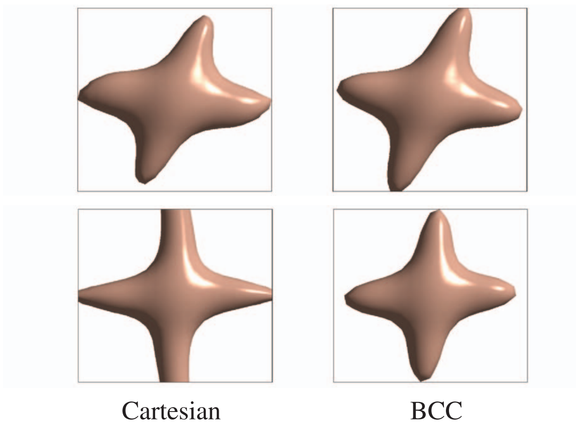

Fig. 2. Visual comparison of the reconstructed $P(\mathbf{r})$. Row 1: $(\theta_1, \theta_2) = (20°, 100°)$, Row 2:$(\theta_1, \theta_2) = (5°, 85°)$. (θ_1,θ_2) are the directions of the two Gaussian components.

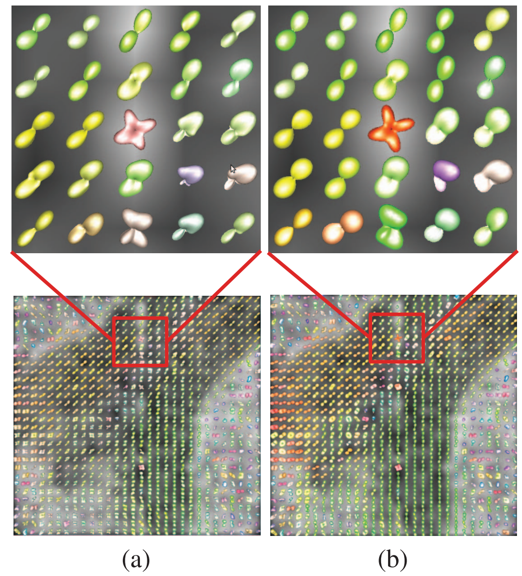

Fig. 3. Probability maps reconstructed from real data set: (a) from Cartesian lattice, (b) from BCC lattice.

5. CONCLUSIONS

This paper introduces the use of optimal sampling in the tomographic reconstruction of the diffusion propagators in DW-MRI. Through comparisons with the traditional Cartesian sampling, we demonstrated that the BCC sampling of the $\mathbf{q}$-space leads to significant improvements in the accuracy of the reconstruction of the diffusion propagator. We also showed that less number of samples on a BCC lattice are required to reconstruct with the same accuracy obtained on a Cartesian lattice.

References

[1] V. Pickalov and P.J. Basser, "3D tomographic reconstruction of the average propagator from MRI data," in *3rd IEEE ISBI*, 2006, pp. 710–713.

[2] P. J. Basser *et al*, "Estimation of the effective self-diffusion tensor from the NMR spin echo.," *JMR B*, vol. 103, pp. 247–254, 1994.

[3] D. S. Tuch *et al*, "High angular resolution diffusion imaging reveals intravoxel white matter fiber heterogeneity," *MRM*, vol. 48(4), pp. 577–582, 2002.

[4] V. J. Wedeen *et al*, "Mapping fiber orientation spectra in cerebral white matter with fourier transform diffusion mri," in *8th ISMRM*, 2000, p. 82.

[5] P.T. Callaghan, *Principles of Nuclear Magnetic Resonance Microscopy*, Clarendon Press, Oxford, 1991.

[6] E. Özarslan and T. H. Mareci, "Generalized DTI and analytical relationships between DTI and HARDI," *MRM*, vol. 50(5), pp. 955–965, 2003.

[7] A. Barmpoutis *et al*, "Regularized positive-definite fourth-order tensor field estimation from DW-MRI," *Neuroimage*, 2009.

[8] M. Descoteaux *et al*, "A fast and robust ODF estimation algorithm in Q-Ball imaging," in *IEEE ISBI*, 2006, pp. 81–84.

[9] B. Jian *et al*, "A novel tensor distribution model for the DWMR signal," in *NeuroImage*, vol. 37(1).

[10] J.D. Tournier *et al*, "Direct estimation of the fiber ODF from DWMRI data using spherical deconv.," *NeuroImage*, vol. 23(3), pp. 1176–1185, 2004.

[11] D. P. Petersen and D. Middleton, "Sampling and reconstruction of wave-number-limited functions in N-dimensional Euclidean spaces," *Information and Control*, vol. 5(4), pp. 279–323, 1962.

[12] H.R. Kunsch *et al*, "Optimal lattices for sampling," *IEEE Tran. Info. Theory*, vol. 51(2), pp. 634–647, 2005.

[13] A. Entezari *et al*, "Practical box splines for reconstruction on the body centered cubic lattice," *IEEE Trans. Vis. Comp. Graph.*, vol. 14, no. 2, pp. 313–328, 2008.

[14] U. Alim and T. Möller, "An FFT with rectangular output on the BCC and FCC lattices," in *Intl Conf. Samp. Theory and Apps.*, 2009.